Environmental Science & Technology

Article

pubs.acs.org/est

Sorption and Redox Reactions of As(III) and As(V) within Secondary Mineral Coatings on Aquifer Sediment Grains

David M. Singer,*[†,∥] Patricia M. Fox,[†] Hua Guo,[‡] Matthew A. Marcus,[§] and James A. Davis[†]

[†]Earth Sciences Division, Lawrence Berkeley National Laboratory, 1 Cyclotron Road, Berkeley, California 94720, United States

[‡]Materials Sciences Division, Lawrence Berkeley National Laboratory, 1 Cyclotron Road, Berkeley, California 94720, United States

[§]Advanced Light Source, Lawrence Berkeley National Laboratory, 1 Cyclotron Road, Berkeley, California 94720, United States

Supporting Information

ABSTRACT: Important reactive phenomena that affect the transport and fate of many elements occur at the mineral−water interface (MWI), including sorption and redox reactions. Fundamental knowledge of these phenomena are often based on observations of ideal mineral−water systems, for example, studies of molecular scale reactions on single crystal faces or the surfaces of pure mineral powders. Much less is understood about MWI in natural environments, which typically have nanometer to micrometer scale secondary mineral coatings on the surfaces of primary mineral grains. We examined sediment grain coatings from a well-characterized field site to determine the causes of rate limitations for arsenic (As) sorption and redox processes within the coatings. Sediments were obtained from the USGS field research site on Cape Cod, MA, and exposed to synthetic contaminated groundwater solutions. Uptake of As(III) and As(V) into the coatings was studied with a combination of electron microscopy and synchrotron techniques to assess concentration gradients and reactive processes, including electron transfer reactions. Transmission electron microscopy (TEM) and X-ray microprobe (XMP) analyses indicated that As was primarily associated with micrometer- to submicrometer aggregates of Mn-bearing nanoparticulate goethite. As(III) oxidation by this phase was observed but limited by the extent of exposed surface area of the goethite grains to the exterior of the mineral coatings. Secondary mineral coatings are potentially both sinks and sources of contaminants depending on the history of a contaminated site, and may need to be included explicitly in reactive transport models.

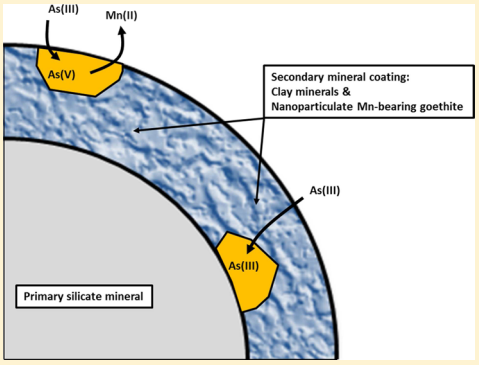

INTRODUCTION

Contaminant transport in the environment is affected by a range of phenomena occurring at the mineral-water interface (MWI), including sorption and diffusion reactions.[1,2] Among the numerous complex biogeochemical factors that could influence these processes at the MWI, the presence of porous, secondary mineral coatings has been shown to play an important role in sorption and contaminant transport through both chemical and physical immobilization in limited flow regimes.[3−6] The presence of porous mineral coatings can directly affect water quality by scavenging metal complexes,[7] controlling nanoparticle transport in confined pore spaces,[8] and controlling the ability of organic matter and microorganisms to adhere to the interface.[9] In comparison to primary minerals, the unique chemical and physical properties of porous mineral coatings can affect their reactivity with respect to contaminant sequestration due to (1) complex and variable porosity, which allows for limited flow potential within confined pore spaces; and (2) a more chemically complex mineralogy and therefore type, abundance and distribution of reactive surface sites. Further, these confined pore spaces may typically dominate the reactive surface area of geologic media.[10] Although porous surface coatings may play a dominant role in limiting contaminant transport compared to the underlying primary mineral grain, the wide variability in the properties of these coatings makes it particularly challenging to build predictive models.[3] This is particularly true when both the sorbent and sorbate contain redox-active species.

An important example of this interplay is arsenic (As) uptake by Fe- and/or Mn-(oxy)hydroxides (e.g., refs 11−13). Arsenic contamination in surface and near-surface environments has a long legacy as a toxin to human and environmental health, from both naturally occurring and anthropogenic sources.[14] Arsenic speciation is a dominant control on its mobility; in general, As(V) adsorption to mineral surfaces is favored at below pH 6, whereas As(III) adsorption is favored at circumneutral pH values.[15] Redox transformations can therefore either promote or limit As retention depending on the surface complex binding strength and available number of reactive sites. Although less abundant than Fe-bearing surface coatings, Mn(III)- and Mn(IV)-bearing phases, such as pyrochroite($Mn(OH)_2$), hausmannite(Mn_3O_4), manganite(γ-MnOOH), birnessite(δ-MnO_2), and Mn-substituted iron oxides[16−19] are likely

Received: June 21, 2013
Revised: August 20, 2013
Accepted: September 16, 2013
Published: September 16, 2013

 © 2013 American Chemical Society

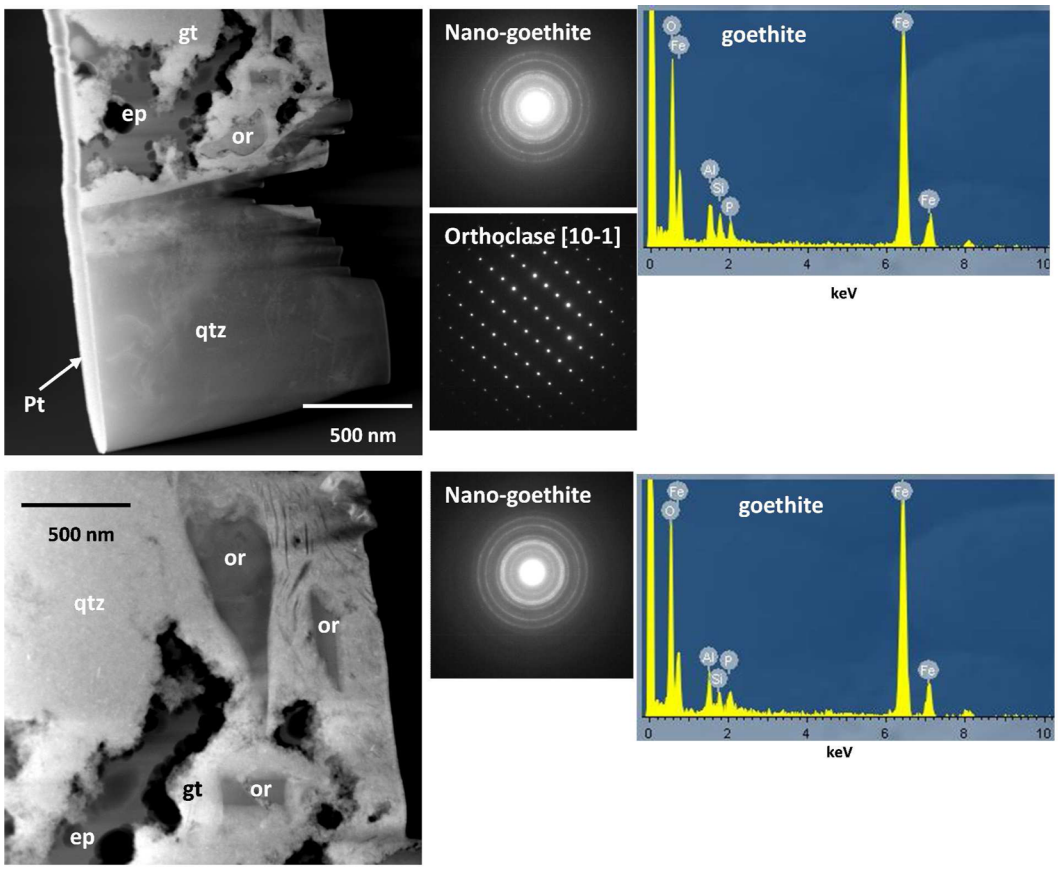

Figure 1. Characteristic TEM dark field images of FIB-extracted coatings samples (left), electron diffraction patterns (middle) and EDS spectra (right). The mineral identification labels are centered at the approximate locations of where the electron diffraction patterns and EDS spectra were collected. The minerals observed here were quartz (qtz), orthoclase (or), and goethite (gt). Also present is the platinum (Pt) band used during FIB liftout and the epoxy (ep) used to mount the sediments in the polished thin sections.

important minerals that provide an abiotic pathway for As(III) oxidation.[12,20] As(III) oxidation by Mn-minerals is dependent on its composition, structure, and crystallinity. In many surface settings, As(III) oxidation by Mn is dependent on the availability of reactive Mn within a trace-Mn-bearing phase such as Mn-substituted goethite.[16] Transport and sorption of As on some spatial and temporal scales may be thermodynamically controlled, where competitive or cooperative effects induced by the presence of other adsorbing ions can influence the adsorption and mobility of As(III) and As(V).[21−24] However, As interactions with mineral surfaces may be kinetically controlled as well, particularly within confined pore spaces.[25] With respect to contaminant transport, these regimes contribute to the immobile fraction of total porosity, as solute transport becomes dominated by diffusion between extragranular and intragranular pore space, driven by concentration gradients.[26,27] The compounding thermodynamic and kinetic effects within these regimes make it particularly challenging to interpret field-based studies of As transport in complex geomedia.

Previous work examining the adsorption and oxidation of As(III) by aquifer materials from five different locations at the USGS research site on Cape Cod, MA, indicated that the extent and rate of As(III) removal from solution increased with increasing solid-phase Mn content, suggesting that Mn-oxides were responsible for the oxidation of As(III).[28] In the current study, we examine As reactions within Mn-bearing bearing secondary mineral coatings using a combination of batch sorption, X-ray microprobe analysis, and electron microscopy, with a goal of determining the dominant phase(s) which control As(III) and As(V) sorption and As(III) oxidation.

■ MATERIALS AND METHODS

Batch Experiments. Kinetic uptake experiments were conducted using aquifer materials collected from the USGS experimental site on Cape Cod, MA. Aquifer sediment (R23AW) was collected from a region of the aquifer characterized by oxic conditions (250−350 μM dissolved oxygen), low dissolved salts (specific conductance <100 μS cm^{-1}), and acidic pH values (pH 4.8−5.8). The R23AW composite is described by Amirbahman et al. (2006).[28] Briefly, this material was a composite made from two cores (R23AWC02 and C03) near USGS well 23A-13 (see Figure 1 in Kent and Fox (2004)[21] for location and details of core sampling and analysis) at an altitude of 13.2 ± 0.4 m above sea level. Core samples were collected using a wire-line core barrel[29] and frozen for transport to the lab where samples were thawed, air-dried, and sieved to <2 mm. For this study, the R23AW composite described by Amirbahman et al. (2006)[28] was further sieved to remove fine-grained particles (<63 μm) by wet sieving with Milli-Q water. This modified composite sample is designated R23AW-SAND; further details about the field site and aquifer properties can be found elsewhere.[6,30−37]

Prior to the batch experiments, the R23AW-SAND was characterized for surface area and bulk composition (SI Tables 1 and 2). Batch experiments were conducted in a Coy

Laboratories, Inc. anaerobic chamber (3% H_2, 97% N_2, < 0.1 ppm O_2). Solutions were bubbled with the anaerobic chamber atmosphere in order to remove dissolved oxygen prior to beginning the experiment. Aquifer sediment (R23AW-SAND) was mixed with a solution of 8 mM NaBr, 1 mM $SrBr_2$, and 0.1 mM As (sodium arsenate or sodium arsenite) which was buffered at pH 5.0 using 3.2 mM sodium acetate and 1.8 mM acetic acid in a sediment suspension of 200 g/L. $SrBr_2$ was included in order to compare the diffusion of ions with different degrees of reactivity into mineral coatings. Although the sediments used in this study were collected from an aerobic aquifer, we kept our experiments anaerobic in order to rule out the possibility of oxygen-mediated oxidation of As. Samples were prepared in duplicate and reacted on an end-overend sample rotator for time periods of 0.5 h to 4 weeks in the dark. At each time point samples were centrifuged, supernatant was removed, and the sediment was immediately frozen in a −80 °C freezer.

Dissolved As speciation was determined on filtered (0.45 μm) solution samples using a strong anion exchange resin[38] by passing 1 mL of solution followed by 10 mL of deionized water through a strong anion exchange resin (Alltech SAX) with an exchange capacity of 0.15 meq/100 mg. The resin was conditioned with 2 mL of methanol followed by 10 mL of deionized water prior to use. At pH 5.0 As(V) is present predominantly as $H_2AsO_4^-$ and is retained by the resin, while As(III) is present predominantly as H_3AsO_3 and elutes through the resin column. As concentrations were measured in the eluted solution for As(III) and in the original solution for total As and Sr by inductively coupled plasma mass spectrometry (ICP-MS; Perkin-Elmer SCIEX Elan DRC II); As(V) was determined by subtraction. Samples were acidified to pH 2 using trace metal grade nitric acid prior to ICP-MS analysis.

Solid samples were freeze-dried and then frozen in a −80 °C freezer prior to thin section preparation. Wet sediment samples were dried and embedded into epoxy (EPO-TEK 301-2FL, Epoxy Technology, Inc.) in an anaerobic chamber, and then allowed to cure under a vacuum for 3 days at room temperature. Once cured, the resin block was removed from the anaerobic chamber and shipped for thin section preparation (Spectrum Petrographics, Inc., Vancouver, WA). Thin sections were polished using kerosene instead of water in order to prevent redox changes from occurring during thin section preparation. Standard thin sections (30 μm thick) were mounted onto quartz slides. Thin sections were stored in an O_2-free environment prior to analysis.

Transmission Electron Microscopy. Secondary mineral coating samples were collected from polished thin sections and further thinned for transmission electron microscopy (TEM) with an FEI Strata 235 Dual Beam focused ion beam (FIB) instrument, using an in situ lift-out technique similar to ones previously described.[39] A Philips CM200 FEG TEM, operated at 200 kV, was used for imaging and EDS chemical analysis; crystalline phases were identified using selected area electron diffraction (SAED) on a JEOL 3010 TEM.

Synchrotron X-ray Microprobe Analysis. Thin sections were prepared from sediments exposed to As(III) and As(V) for 0.5, 2, and 24 h for micro-X-ray fluorescence (μ-XRF) measurements at beamlines 2−3 at the Stanford Synchrotron Radiation Laboratory (SSRL), 10.3.2[40,41] at the Advanced Light Source (ALS), and 13-IDE[42] at the Advanced Photon Source (APS). Description of the experimental setup and data processing protocols for these experiments can be found in the Supporting Information (SI).

RESULTS AND DISCUSSION

Mineral Coating Characterization. The mineralogy and texture of the secondary mineral coatings was determined by TEM analysis of FIB-extracted samples (Figure 1 and SI Figure 1). The primary mineral grains were dominated by crystalline quartz with some orthoclase present. The uneven secondary coatings ranged from nearly absent to up to 25 μm thick. The coatings are highly porous with numerous voids (filled with epoxy in the thin sections). Elemental mapping and electron diffraction indicated two dominant compositional zones that are heterogeneously mixed within the coatings: (1) Al/Si-rich and (2) Fe-rich. The Al/Si-rich zones were found to be dominated by micrometer- to submicrometer orthoclase grains and poorly crystalline to amorphous material with a clay-like composition. The fabric, bulk composition, and association with the feldspar grains of these phases are consistent with illite, chlorite and allophane observed in similar samples of Cape Cod sediments.[6] The Fe-rich zones were found to be dominated by nanoparticulate goethite with minor ilmenite (Figure 1 and SI Figure 1). The nanoparticulate goethite is present as micrometer-scale aggregates intricately mixed with the Al/Si-rich phases, whereas ilmenite was observed mostly as larger aggregates separated and more delineated from the Al/Si-rich zones. The goethite was found to contain Al and P based on EDS analysis, consistent with previous observations.[6] XMP analysis consistently found trace Mn and Ti within the Fe-rich zones of the coatings as well (Figure 2 and SI Figures 3, 4, 5, and 6). It is not surprising that trace Mn would be absent during analysis by traditional XRF measurements with detection limits ∼0.01 wt.%,[43] in contrast to synchrotron-based μ-XRF analyses that can detect in the 50−100 ng/g range for many elements at third-generation synchrotron facilities.[44] In these elemental maps, the presence of Ti could be due to a mixture of ilmenite and goethite; the occurrence of a Ti-bearing goethite could not be exclusively determined. Further, although the TEM EDS analysis indicated that Mn was a trace constituent in ilmenite, the XMP analysis showed that nearly all Fe-rich zones within the coatings contained trace Mn. Given the relative abundance of the nanoparticulate goethite compared to the ilmenite, it is likely that the dominant Mn-bearing phase within the Fe-rich zones is nanoparticulate goethite. There was no TEM or XMP evidence for a Mn-(hydro)oxide or dominantly Mn-bearing phase, and the role of this Mn-bearing goethite phase in As redox transformations will be discussed below.

As(III) and As(V) Batch Sorption. Uptake of As(III) and As(V) from solution onto the R23AW-SAND composite was measured at pH 5 for up to 700 h (Figure 3). Uptake of 40% of aqueous As(V) occurred within 24 h, followed by slower uptake. Complete removal of As(V) from solution occurred by 700 h, corresponding to a solid phase concentration of 0.49 μmol/g. In contrast, As(III) sorption was much lower; only 30% of the As(III) was removed from solution after 700 h, corresponding to 0.18 μmol/g, some of which could be As(III) oxidized to sorbed As(V). At pH 5, As(V) sorption onto many mineral phases, including clay minerals and Al-oxides is much greater than As(III) sorption.[45] However, As(III) and As(V) sorption onto goethite is similar at pH 5.[11,46,47] Thus the greater level of As(V) sorption observed in this experiment could be due to two possible effects. First, goethite may not be

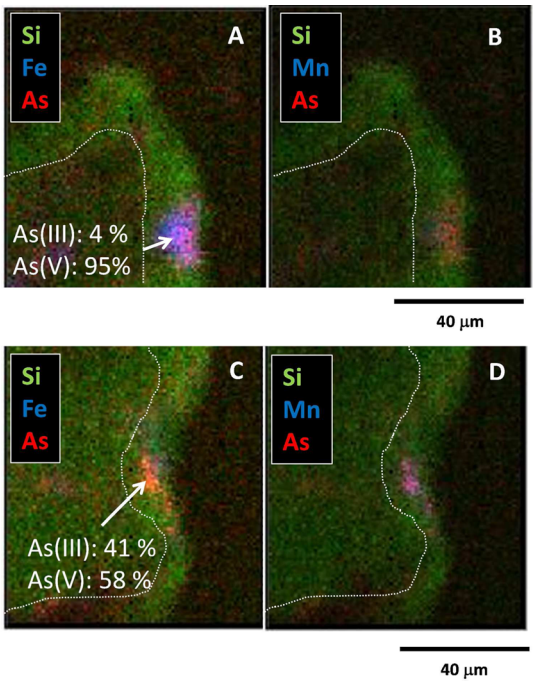

Figure 2. Characteristic XMP images (collected at SSRL beamline 2–3) of the edges of two areas (A-B and C-D) of one quartz grain in a polished thin section, highlighting the amount of remaining As(III), from μ-XANES analysis, associated with an Mn-bearing Fe-rich phase (likely nanoparticulate goethite). The amount of As(III) remaining is related to the extent of available surface area in contact with the exterior of the mineral coating (the blackish area is epoxy and denotes the original grain surface/solution contact). This sample was exposed to As(III) for 30 min. Additional element maps of this grain are shown in the top panel SI Figure 3. The dashed white lines denote the boundary between the primary mineral grain and the coatings.

the only sorbent phase for As; XMP analyses indicated that although As was primarily associated with the Fe-rich zones within the coatings, some diffuse As was associated with the Al/Si-rich phases and preferential sorption of As(V) over As(III) to these clay minerals could account for the sorption behavior. Second, natural goethite has different sorbing properties compared to the synthetic analogues typically used in laboratory experiments, for example, adsorbed silicate or Al-substitution within the mineral structure. The low level of As(III) adsorption is consistent with that observed by Amirbahman et al. (2006) for this sample (without sieving).

In the case of As(III), slow, nonfirst order uptake kinetics may reflect a combination of diffusion, sorption, and oxidation to As(V) by Mn-bearing minerals within the coatings. Unlike Cape Cod sediments with higher Mn contents, in which As(III) oxidation dominated uptake compared to sorption, Amirbahman et al. (2006) noted that sorption of As(III) was the dominant mechanism of As(III) removal by R23AW over the entire concentration range investigated (28.5–500.3 μM), with approximately one-third of the solid-bound As present as As(V) for an initial As(III) concentration of 85 μM. Arsenic adsorption kinetics on iron oxides also show a pH dependence, with faster adsorption occurring at below pH 6 for As(V) and above pH 7 for As(III),[47,48] consistent with our data. Slow As uptake kinetics compared to those observed in pure mineral suspensions underscore the importance of diffusion controls in the microporous structure of secondary mineral coatings in natural samples.

As Speciation and Distribution in Mineral Coatings. XMP analysis of polished thin sections of R23AW-SAND after exposure to $As(III)_{aq}$ and $As(V)_{aq}$ for 0.5, 2, and 24 h indicated that As distribution was dominated by association with Fe-bearing phases in the coatings; XMP analyses are presented for As(III) reacted for 0.5 h (Figure 1, SI Figure 2, 3, 9, and 10), 2 h (SI Figure 4), and 24 h (SI Figure 5), and As(V) reacted for 24 h (SI Figure 6). These Fe-rich phases range from approximately 0.1–10 μm in thickness, and were consistently observed within secondary mineral coatings on primary Si-bearing grains identified as quartz and feldspar by TEM analysis. The boundary between the primary mineral grain and the secondary coating could be delineated in the XMP analyses (note the dashed lines in Figure 2) by the spatial distribution of Si- and metal-rich regions zones on the exterior of mineral grains; the transition between these zones were consistent with textural and grain size transition observed by reflected light microscopy and TEM. The elemental distribution and grain boundary morphologies paralleled the TEM results; Si- and Fe-rich regions are consistent with nanoparticulate goethite intricately mixed with clay-like secondary minerals. Attempts

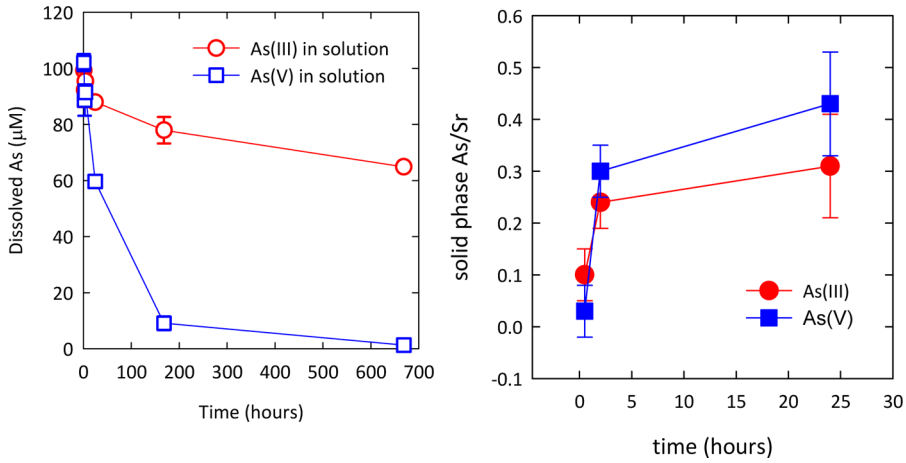

Figure 3. (A) Batch sorption results versus time showing dissolved As(III) or As(V) remaining in solution. Initial As(III) or (V) concentrations were 100 μM. (B) Estimated solid phase As/Sr values based on XMP analysis; the amount of solid phase As and Sr was determined by normalizing the fluorescence counts to I_0 and summing the total counts in a given elemental map. Error bars represent two standard deviation values.

to collect microdiffraction patterns to identify specific mineral grains proved unsuccessful in the experimental geometry for which most of the data was collected. However, given the similarities in bulk element composition observed by XMP and TEM analyses, it is likely that the As-bearing phase observed in the XMP analyses is dominated by nanoparticulate goethite. Consistent with the TEM analysis of the coatings, the Si-rich areas (shown above to be dominated by illite, chlorite, and allophane) were often intertwined with the Fe-rich zones. In some cases, the Si-rich zones completely encapsulated the Fe-rich grains, whereas in other cases the Fe-rich grains were exposed at the exterior of the coatings and directly adjacent to the epoxy.

The solid phase As concentration of the R23AW-SAND after exposure to As(III) and As(V) was estimated by comparing the total fluorescence counts in a given element map normalized to the beam flux (I_0). Further, the rate of As(III) and As(V) sorption and diffusion into the mineral coatings was compared by determining the ratio of As to strontium (Sr), added to the solution prior to exposure to the R23AW-SAND. The amount of Sr removed from solution reached a near steady-state within 0.5 h of exposure (SI Figure 7), which is supported by the lack of change in the solid-phase Sr fluorescence counts in the XMP analysis. It is possible that the differences in dissolved Sr concentrations are due to a small electrostatic effect during As(V) and As(III) sorption. However, given the small difference between the dissolved Sr concentrations in the two systems (0.01−0.07 mM) and the associated errors (standard deviations are 0.01−0.03 mM) it is difficult to determine whether this effect is significant. In contrast to As, Sr was spatially associated with both the Fe-rich and Al/Si-rich grains within the mineral coatings (SI Figure 4, 5, 6). This suggests that Sr quickly diffuses into the mineral coatings and is partitioned to most of the mineral phases present, whereas As preferentially adsorbs onto Fe-oxides. In contrast, movement of As(III) and As(V) into the interior of the coatings is slower than Sr as evidenced by the sorption trends and the As/Sr ratio in the solid phase over time (Figure 3A and B). Given the relatively constant solid phase Sr concentration, the increase in the As/Sr values is consistent with the removal of As(III) and As(V) from solution and slower diffusion into the mineral coatings caused by significant sorption to the surfaces of minerals within the coating regime.

Micro-XANES spectra collected at As-bearing Fe-rich regions indicated that both As(III) and As(V) were present at varying ratios (SI Figure 8) when R23AW-SAND was exposed to As(III). In addition to the μ-XANES spectra, As redox maps were also collected to determine the spatial distribution of As(III) and As(V) on R23AW-SAND (SI Figure 9) after exposure to $As(III)_{aq}$ for 30 min. These analyses showed that As associated with Fe-grains near the mineral coating exterior was dominated by As(V). In contrast, As associated with Fe-grains in the interior of coatings or near the coating exterior but surrounded by Si-rich grains was more likely to be a mixture of As(III) and As(V). The amount of exposed surface area of the Fe-grains at the exterior of the mineral coating was measured on all As-bearing grains analyzed by XMP, and was determined by counting pixels of the Fe-grains in contact with epoxy for all analyzed grains. The exposure of these grains near the exterior of the coating was directly proportional to the amount of As(III) remaining (Figure 4), demonstrating the possible importance of diffusion-limited migration of reactants or products with respect to As(III) oxidation associated with the goethite.

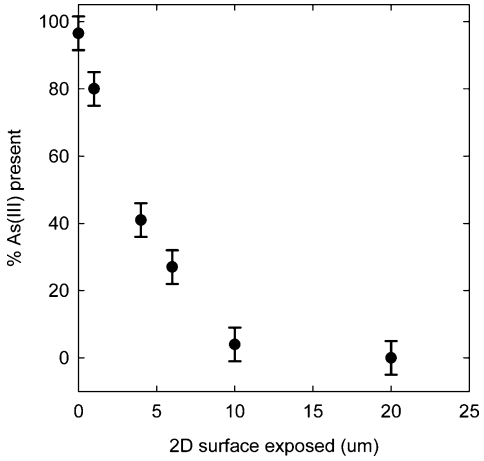

Figure 4. The amount of exterior surface area of the Mn-bearing nanoparticulate goethite exposed to the exterior of the mineral coating versus the percent As(III) present compared to total As, based on XMP analysis of R23AW-SAND after exposure to $As(III)_{aq}$ for 30 min.

The Fe-rich grains were consistently found to contain trace concentrations of Mn (Figure 2). Attempts were made to collect Mn K-edge bulk- and μ-XANES spectra and to collect Mn redox speciation maps; however, the Mn concentration was too low to definitively determine if As(III) oxidation was coupled to Mn redox changes. However, since As was only associated with the goethite-dominated Fe-rich grains, it is likely that As(III) oxidation occurred on those mineral surfaces. XMP analyses did show that a mixed-valence Mn-bearing phase is present in these Fe-rich grains (SI Figure 10). Oxidation of As(III) to As(V) by Fe(III) is a thermodynamically favorable reaction at below pH 6 but kinetically limited at circumneutral pH.[49] Pure, Mn-free goethite has been shown to be unable to oxidize As(III), whereas oxidation of As(III) to As(V) occurred by Mn-substituted goethite.[16] Synthetic Mn-substituted goethite was first examined prior to observations of naturally occurring Mn-substituted goethite,[17] and early work suggested that Mn was dominantly in the tetravalent state.[50] More recent work has shown that Mn resides dominantly in the trivalent oxidation state in Mn-substituted goethite samples,[18,19] which impacts thermodynamic calculations aimed at predicting the oxidizing potential of the Mn-bearing phase. Ultimately, the presence of Mn in goethite has been shown to play a critical role with respect to As redox transformations, and dependent on the release of soluble Mn(II); Sun et al. (1999) have suggested that complete oxidation of As(III) by Mn-bearing goethite might be limited due to the role of produced Mn(II).[16] Although the mechanism for the two electron transfer has not been uniquely determined, given the electronic configuration of Mn(III), it is likely that Mn-substituted goethite acts as a p-type semiconductor.[51] Electrons accepted from As(III) oxidation by Mn-substituted goethite may be delocalized over the solid instead of associated with a specific surface atom. Therefore, only those electrons of Mn(II) on the surface may be desorbed and released to the solution. Although we could not definitely determine that Mn in the goethite grains is responsible for As(III) oxidation, this behavior may explain why we observed that goethite grains in closer proximity to the exterior of the mineral coating and with more surface area exposed had lower

amounts of As(III) remaining, that is, if As(III) oxidation requires release of Mn(II) to solution, goethite grains buried within the coating would limit Mn(II) diffusion out and allow for more As(III) to remain. Further, it is unlikely that changes in dissolved Mn would be detected; in similar experiments conducted on the same material, Amirbahman et al. (2006) found dissolved Mn concentrations to be below detection limits even when As(III) oxidation was clearly detected, (based on measured As(V) production, which they attributed the lack of dissolved Mn to Mn(II) sorption.[28]

ENVIRONMENTAL IMPLICATIONS

There have been few attempts to apply the spatial resolution and sensitivity of TEM and X-ray microprobe techniques to determine spatial gradients of sorbing reactants within secondary mineral coatings. The combination of μ-XRF element mapping and μ-XANES spectroscopy, using reacted mineral grains and FIB-extracted samples of the grain-coating contact provides a significant new approach to studying reactive processes within the coating regime. This is highlighted by the observation that in the absence of evidence for other oxidants, Mn present at trace levels in the nanoparticulate goethite is likely responsible for As(III) oxidation; which could not have been determined without this suite of techniques. In the absence of these data, previous studies have assumed that discrete Mn-oxide particles must be the primary As(III)-oxidizing phase.[28] The results obtained in this study suggest that oxidation of As(III) and natural attenuation in aquifer sediments may be limited in rate and extent by the lack of reactive surface area of oxidizing surfaces in complex secondary mineral surface coatings. Furthermore, the results show that potential diffusion, retarded by sorption to surfaces within the network of pore space within secondary grain coatings, must be slow and thus constrain the attainment of equilibrium for sorption of As(V). These results highlight the importance of future work to quantify diffusion constraints for mineral surface reactions within conceptual models for reactive contaminant transport.[2] Secondary mineral coatings are potentially both sinks and sources of contaminants depending on the history of a contaminated site, and may play an important role in determining whether equilibrium versus kinetic reactive transport models should be used in simulating long-term reactive transport at contaminated sites.[52] Whether the diffusion limitation within coatings is rate-determining depends on the specifics of flow and aquifer sediment structure at specific field sites, but in some cases such diffusion limitations could be significant in determining field scale contaminant transport.

ASSOCIATED CONTENT

Supporting Information

Additional information for sediment characterization, XMP element maps, and micro-XANES spectra is included. This material is available free of charge via the Internet at http://pubs.acs.org.

AUTHOR INFORMATION

Corresponding Author

*(D.M.S.) E-mail: dsinger4@kent.edu.

Present Address

‖Department of Geology, Kent State University

Notes

The authors declare no competing financial interest.

ACKNOWLEDGMENTS

We gratefully acknowledge support from the Laboratory Directed Research and Development (LDRD) and Sustainable Systems (SS) Scientific Focus Area (SFA) funding at Lawrence Berkeley National Laboratory, provided by the Director, Office of Science, of the U.S. Department of Energy under Contract No. DE-AC02-05CH11231. Portions of this work were carried out at the Stanford Synchrotron Radiation Lightsource (SSRL) and the National Center for Electron Microscopy (NCEM) at Lawrence Berkeley National Laboratory (LBNL). We thank Joern Larsen (LBL) for ICP analyses, Nazila Kaviani (USGS) for BET analyses, and Sam Webb (SSRL), Benjamin Kocar (SSRL), Matthew Newville (APS), Joanne Stubbs (APS), and Ruth Tinnacher (LBL) for XMP data collection assistance. SSRL is a Directorate of SLAC National Accelerator Laboratory and an Office of Science User Facility operated for the U.S. Department of Energy Office of Science by Stanford University. Use of the Advanced Photon Source, an Office of Science User Facility operated for the U.S. Department of Energy (DOE) Office of Science by Argonne National Laboratory, was supported by the U.S. DOE under Contract No. DE-AC02-06CH11357. The Advanced Light Source is supported by the Director, Office of Science, Office of Basic Energy Sciences, of the U.S. Department of Energy under Contract No. DE-AC02-05CH11231. NCEM is supported by the U.S. Department of Energy under Contract No. DE-AC02-05CH11231. Comments from three anonymous reviewers improved this manuscript.

REFERENCES

(1) Brown, G. E., Jr.; Parks, G. A. Sorption of trace elements on mineral surfaces: Modern perspectives from spectroscopic studies, and comments on sorption in the marine environment. *Int. Geol. Rev.* **2001**, *43* (11), 963−1073.

(2) Fox, P. M.; Davis, J. A.; Hay, M. B.; Conrad, M. E.; Campbell, K. M.; Williams, K. H.; Long, P. E. Rate-limited U(VI) desorption during a small-scale tracer test in a heterogeneous uranium-contaminated aquifer. *Water Resour. Res.* **2012**, *48* (5), W05512.

(3) Davis, J. A.; Meece, D. E.; Kohler, M.; Curtis, G. P. Approaches to surface complexation modeling of uranium(VI) adsorption on aquifer sediments. *Geochim. Cosmochim. Acta* **2004**, *68* (18), 3621−3641.

(4) Stubbs, J. E.; Veblen, L. A.; Elbert, D. C.; Zachara, J. M.; Davis, J. A.; Veblen, D. R. Newly recognized hosts for uranium in the Hanford Site vadose zone. *Geochim. Cosmochim. Acta* **2009**, *73* (6), 1563−1576.

(5) Penn, R. L.; Zhu, C.; Xu, H.; Veblen, D. R. Iron oxide coatings on sand grains from the Atlantic coastal plain: High-resolution transmission electron microscopy characterization. *Geology* **2001**, *29* (9), 843−846.

(6) Zhang, S.; Kent, D. B.; Elbert, D. C.; Shi, Z.; Davis, J. A.; Veblen, D. R. Mineralogy, morphology, and textural relationships in coatings on quartz grains in sediments in a quartz-sand aquifer. *J. Contam. Hydrol.* **2011**, *124* (1−4), 57−67.

(7) Davis, J. A.; Kent, D. Surface complexation modeling in aqueous geochemistry. *Rev. Mineral. Geochem.* **1990**, *23* (1), 177−260.

(8) Chowdhury, I.; Hong, Y.; Honda, R. J.; Walker, S. L. Mechanisms of TiO_2 nanoparticle transport in porous media: Role of solution chemistry, nanoparticle concentration, and flowrate. *J. Colloid Interface Sci.* **2011**, *360* (2), 548−555.

(9) Harvey, R. W.; Metge, D. W.; Barber, L. B.; Aiken, G. R. Effects of altered groundwater chemistry upon the pH-dependency and magnitude of bacterial attachment during transport within an organically contaminated sandy aquifer. *Water Res.* **2010**, *44* (4), 1062−1071.

(10) Wang, Y.; Bryan, C.; Xu, H.; Gao, H. Nanogeochemistry: Geochemical reactions and mass transfers in nanopores. *Geology* **2003**, *31* (5), 387−390.
(11) Manning, B. A.; Fendorf, S. E.; Goldberg, S. Surface structures and stability of arsenic(III) on goethite: Spectroscopic evidence for inner-sphere complexes. *Environ. Sci. Technol.* **1998**, *32* (16), 2383−2388.
(12) Manning, B. A.; Fendorf, S. E.; Bostick, B.; Suarez, D. L. Arsenic(III) oxidation and arsenic(V) adsorption reactions on synthetic birnessite. *Environ. Sci. Technol.* **2002**, *36* (5), 976−981.
(13) Fendorf, S.; Eick, M. J.; Grossl, P.; Sparks, D. L. Arsenate and chromate retention mechanisms on goethite. 1. Surface structure. *Environ. Sci. Technol.* **1997**, *31* (2), 315−320.
(14) Graeme, Md, K. A.; Pollack, M. D. F. C. V., Jr. Heavy metal toxicity, part I: Arsenic and mercury. *J. Emerg. Med.* **1998**, *16* (1), 45−56.
(15) Bissen, M.; Frimmel, F. H. Arsenic—A review. Part I: Occurrence, toxicity, speciation, mobility. *Acta Hydrochim. Hydrobiol.* **2003**, *31* (1), 9−18.
(16) Sun, X.; Doner, H. E.; Zavarin, M. Spectroscopy study of arsenite [As(III)] oxidation on Mn-substituted goethite. *Clays Clay Miner.* **1999**, *47* (4), 474−480.
(17) Stiers, W.; Schwertmann, U. Evidence for manganese substitution in synthetic goethite. *Geochim. Cosmochim. Acta* **1985**, *49* (9), 1909−1911.
(18) Scheinost, A. C.; Stanjek, H.; Schulze, D. G.; Gasser, U.; Sparks, D. L. Structural environment and oxidation state of Mn in goethite-groutite solid-solutions. *Am. Mineral.* **2001**, *86* (1−2), 139−146.
(19) Singh, B.; Sherman, D. M.; Gilkes, R. J.; Wells, M. A.; Mosselmans, J. F. W. Incorporation of Cr, Mn and Ni into goethite (α-FeOOH): Mechanism from extended X-ray absorption fine structure spectroscopy. *Clay Minerals* **2002**, *37* (4), 639−649.
(20) Hem, J. D. Redox processes at surfaces of manganese oxide and their effects on aqueous metal ions. *Chem. Geol.* **1978**, *21* (3−4), 199−218.
(21) Kent, D.; Fox, P. The influence of groundwater chemistry on arsenic concentrations and speciation in a quartz sand and gravel aquifer. *Geochem. Trans.* **2004**, *5* (1), 1−12.
(22) Liu, F.; De Cristofaro, A.; Violante, A. Effect of pH, phosphate and oxalate on the adsorption/desorption of arsenate on/from goethite. *Soil Sci.* **2000**, *166*, 197−208.
(23) Höhn, R.; Isenbeck-Schröter, M.; Kent, D. B.; Davis, J. A.; Jakobsen, R.; Jann, S.; Niedan, V.; Scholz, C.; Stadler, S.; Tretner, A. Tracer test with As(V) under variable redox conditions controlling arsenic transport in the presence of elevated ferrous iron concentrations. *J. Contam. Hydrol.* **2006**, *88* (1−2), 36−54.
(24) Stadler, S.; Jann, S.; Höhn, R.; Isenbeck-Schröter, M.; Niedan, V.; Scholz, C.; Tretner, A.; Davis, J.; Kent, D. Tracer tests with As-(III) in the oxic and suboxic groundwater zones at the USGS Cape Cod site, Mass., USA. In *Water-Rock Interaction. WRI-10*; AA Balkema Publishers: Rotterdam, The Netherlands, 2001, 1013−1016.
(25) Masue-Slowey, Y.; Kocar, B. D.; Bea Jofré, S. A. s.; Mayer, K. U.; Fendorf, S. Transport implications resulting from internal redistribution of arsenic and iron within constructed soil aggregates. *Environ. Sci. Technol.* **2010**, *45* (2), 582−588.
(26) Hay, M. B.; Stoliker, D. L.; Davis, J. A.; Zachara, J. M. Characterization of the intragranular water regime within subsurface sediments: Pore volume, surface area, and mass transfer limitations. *Water Resour. Res.* **2011**, *47* (10), W10531.
(27) Sammartino, S.; Bouchet, A.; Prêt, D.; Parneix, J. C.; Tevissen, E. Spatial distribution of porosity and minerals in clay rocks from the Callovo-Oxfordian formation (Meuse/Haute-Marne, Eastern France)—implications on ionic species diffusion and rock sorption capability. *Appl. Clay Sci.* **2003**, *23* (1−4), 157−166.
(28) Amirbahman, A.; Kent, D. B.; Curtis, G. P.; Davis, J. A. Kinetics of sorption and abiotic oxidation of arsenic(III) by aquifer materials. *Geochim. Cosmochim. Acta* **2006**, *70* (3), 533−547.
(29) Zapico, M. M.; Vales, S.; Cherry, J. A. A wireline piston core barrel for sampling cohesionless sand and gravel below the water table. *Ground Water Monit. Rem.* **1987**, *7* (3), 74−82.
(30) Barber, L. B., II; Thurman, E. M.; Runnells, D. D. Geochemical heterogeneity in a sand and gravel aquifer: Effect of sediment mineralogy and particle size on the sorption of chlorobenzenes. *J. Contam. Hydrol.* **1992**, *9* (1−2), 35−54.
(31) Bau, M.; Alexander, B.; Chesley, J. T.; Dulski, P.; Brantley, S. L. Mineral dissolution in the Cape Cod aquifer, Massachusetts, USA: I . Reaction stoichiometry and impact of accessory feldspar and glauconite on strontium isotopes, solute concentrations, and REY distribution. *Geochim. Cosmochim. Acta* **2004**, *68* (6), 1199−1216.
(32) Coston, J. A.; Fuller, C. C.; Davis, J. A. Pb^{2+} and Zn^{2+} adsorption by a natural aluminum- and iron-bearing surface coating on an aquifer sand. *Geochim. Cosmochim. Acta* **1995**, *59* (17), 3535−3547.
(33) Davis, J. A.; Coston, J. A.; Kent, D. B.; Fuller, C. C. Application of the surface complexation concept to complex mineral assemblages. *Environ. Sci. Technol.* **1998**, *32* (19), 2820−2828.
(34) LeBlanc, D. R.; Garabedian, S. P.; Hess, K. M.; Gelhar, L. W.; Quadri, R. D.; Stollenwerk, K. G.; Wood, W. W. Large-scale natural gradient tracer test in sand and gravel, Cape Cod, Massachusetts: 1. Experimental design and observed tracer movement. *Water Resour. Res.* **1991**, *27* (5), 895−910.
(35) Wood, W. W.; Kraemer, T. F.; Hearn, P. P. Intragranular diffusion: An important mechanism influencing solute transport in clastic aquifers? *Science* **1990**, *247* (4950), 1569−1572.
(36) Kent, D. B.; Abrams, R. H.; Davis, J. A.; Coston, J. A.; Leblanc, D. R. Modeling the influence of variable pH on the transport of zinc in a contaminated aquifer using semiempirical surface complexation models. *Water Resour. Res.* **2000**, *36* (12), 3411−3425.
(37) Davis, J. A.; Kent, D. B.; Coston, J. A.; Hess, K. M.; Joye, J. L. Multispecies reactive tracer test in an aquifer with spatially variable chemical conditions. *Water Resour. Res.* **2000**, *36* (1), 119−134.
(38) Bednar, A. J.; Garbarino, J. R.; Ranville, J. F.; Wildeman, T. R. Preserving the distribution of inorganic arsenic species in groundwater and acid mine drainage samples. *Environ. Sci. Technol.* **2002**, *36* (10), 2213−2218.
(39) Giannuzzi, L. A.; Kempshall, B. W.; Schwartz, S. M.; Lomness, J. K.; Prenitzer, B. I.; Stevie, F. A., FIB lift-out specimen preparation techniques: Ex-situ and in-situ methods. In *Focused Ion Beams: Instrumentation, Theory, Techniques and Practice*; Giannuzzi, L. A., Stevie, F. A., Eds.; Springer: New York, 2005; pp 201−228.
(40) Marcus, M. A.; MacDowell, A. A.; Celestre, R.; Manceau, A.; Miller, T.; Padmore, H. A.; Sublett, R. E. Beamline 10.3.2 at ALS: A hard X-ray microprobe for environmental and materials sciences. *J. Synchrotron Rad.* **2004**, *11* (3), 239−247.
(41) Marcus, M. A. X-ray photon-in/photon-out methods for chemical imaging. *TrAC, Trends Anal. Chem.* **2010**, *29* (6), 508−517.
(42) Newville, M.; Sutton, S. R.; Rivers, M. L.; Eng, P. Micro-beam x-ray absorption and fluorescence spectroscopies at GSECARS: APS beamline 13ID. *J. Synchrotron Rad.* **1999**, *6* (3), 353−355.
(43) Dunham, A. C.; Wilkinson, F. C. F. Accuracy, precision and detection limits of energy-dispersive electron-microprobe analyses of silicates. *X-ray Spectrom.* **1978**, *7* (2), 50−56.
(44) Bertsch, P. M.; Hunter, D. B. Applications of synchrotron-based X-ray microprobes. *Chem. Rev.* **2001**, *101* (6), 1809−1842.
(45) Goldberg, S. Competitive adsorption of arsenate and arsenite on oxides and clay minerals contribution from the George E. Brown Jr., Salinity Laboratory. *Soil Sci. Soc. Am. J.* **2002**, *66* (2), 413−421.
(46) Dixit, S.; Hering, J. G. Comparison of arsenic(V) and arsenic(III) sorption onto iron oxide minerals: Implications for arsenic mobility. *Environ. Sci. Technol.* **2003**, *37* (18), 4182−4189.
(47) Waltham, C. A.; Eick, M. J. Kinetics of arsenic adsorption on goethite in the presence of sorbed silicic acid. *Soil Sci. Soc. Am. J.* **2002**, *66* (3), 818−825.
(48) Raven, K. P.; Jain, A.; Loeppert, R. H. Arsenite and arsenate adsorption on ferrihydrite: Kinetics, equilibrium, and adsorption envelopes. *Environ. Sci. Technol.* **1998**, *32* (3), 344−349.

(49) Oscarson, D. W.; Huang, P. M.; Liaw, W. K. The oxidation of arsenite by aquatic sediments 1. *J. Environ. Qual.* **1980**, *9* (4), 700−703.
(50) Manceau, A.; Gorshkov, A. I.; Drits, V. A. Structural chemistry of Mn, Fe, Co, and Ni in manganese hydrous oxides; Part I, information from XANES spectroscopy. *Am. Mineral.* **1992**, *77* (11−12), 1133−1143.
(51) Bockris, J. M.; Reddy, A.; Vijh, A. K. Modern electrochemistry. *J. Electrochem. Soc.* **1972**, *119*, 136C.
(52) Yabusaki, S. B.; Fang, Y.; Waichler, S. R. Building conceptual models of field-scale uranium reactive transport in a dynamic vadose zone-aquifer-river system. *Water Resour. Res.* **2008**, *44* (12), W12403.

Sorption and Redox Reactions of As(III) and As(V) within Secondary Mineral Coatings on Aquifer Sediment Grains

David M. Singer[*1], *Patricia M. Fox*[1], *Hua Guo*[2], *Matthew A. Marcus*[3], *James A. Davis*[1]

1. Earth Sciences Division, Lawrence Berkeley National Laboratory

2. Materials Sciences Division, Lawrence Berkeley National Laboratory

3. Advanced Light Source, Lawrence Berkeley National Laboratory

*Corresponding author: dsinger4@kent.edu

* Current address: Department of Geology, Kent State University

Submitted to Environmental Science & Technology 6/21/13

Revised and resubmitted 08/20/13

Supporting Information

Experimental setup of synchrotron x-ray microprobe analysis

The synchrotron x-ray beam size used for the μ-XRF images was 2 μm x 2 μm (APS and SSRL) and 3 μm x 3 μm (ALS) at full width half-maximum using a Pt-coated Kirkpatrick-Baez (K-B) focusing optics system (XRadia). X-ray fluorescence data was collected using a single-element (SSRL) and four-element (APS) Si Vortex Detector (SSI) and seven-element Ge solid-state fluorescence detector (XIA) (ALS). Monochromatic x-rays were selected using a water cooled Si(111) $\varphi = 90$ double crystal monochromator. All data were collected at 1 μm pixel size and 50 ms dwell time per point. The x-ray energy was calibrated to the maximum of the first derivative of a sodium arsenate, As(V), sample spectrum and set at 11869.7 eV. Element maps were collected for the following major and minor/trace elements: As, Ca, Fe, K, Mn, S, Si, Sr, Ti, and Zn. Fluorescence maps were analyzed using the Microanalysis Toolkit.[1] Quantitative determination of As(V) and As(III) at selected locations within the thin sections was accomplished using As K-edge micro-X-ray absorption near-edge structure (μ-XANES) spectroscopy (SSRL); scans were collected from 200 eV below to 300 eV above the As K-edge. Linear combination XANES spectral fitting was performed using SIXPACK[2] to determine the proportion of As(V) to As(III) while minimizing reduced chi square values. Sodium arsenite and sodium arsenate were used as As(III) and As(V) standards for both micro-XANES spectroscopy and As redox mapping, respectively. Arsenic redox mapping (SSRL), following previous methods[3, 4] was performed by collecting maps at 11860 eV, 11872 keV, 11875 keV, and 11880 keV to determine the distribution of As(III) and As(V), and below the Fe K-edge (at 7 keV) to differentiate Mn and Fe spatial distribution. Based on the three As maps, the spatial distribution of As(III), As(V) and total As was based on doing a linear combination fit to the intensity of each pixel as a function of energy. For data from all beamlines, fluorescence counts were normalized to the measured intensity of the incident energy of the x-ray beam (I_0) for each energy map across each line; I_0 did not change (within 1 %) over each map area and for each energy.

For data collected at beamline 10.3.2 at the Advanced Light Source (SI Figure 10), arsenic maps were collected at 11835 eV, 11870 eV, 11873.6 eV, and 11902 eV. Manganese maps were collected at 6530 eV, 6544 eV, 6547 eV, 6552.7 eV, 6555.8 eV, and 6670 eV. Total Fe distribution was collected at 13000 eV. XMP data were acquired with procedures similar to those described in Marcus et al. (2010).[5] Briefly, Mn-bearing reference standards used for the redox mapping included an aqueous $Mn(II)SO_4$ solution, manganite [Mn(III)O(OH)], and ramsdellite [$Mn(IV)O_2$].[6] Additional Mn-bearing references used for comparison were Mn(II) sorbed on fungal biomass and a Mn(IV)-phyllomangate. Redox maps were created by doing a principle component analysis of each pixel in the image based on the six energy values the maps were collected.

Although we did not determine if the EPO-TEK 301-2FL resin reacted with As in the sample and potentially changed the As speciation within the epoxy-embedded samples, previous work using the same resin, similar As concentrations and media, and beamline experimental setup has shown that the resin does not react with or impact the As oxidation state.[7, 8] Further, it is reasonable to assume that this lack of reactivity is true for other redox sensitive elements and compounds.[9, 10]

SI Table 1: R23AW-SAND composite surface area, determined by 10-point N_2-BET analysis (QuantaChrome Autosorb-1-MP gas sorption analyzer). The average surface area is 0.32 ± 0.047 m^2/g.

Replicate	**C parameter**	**Surface Area (m^2/g)**
1	287.55	0.36
2	342.93	0.34
3	323.78	0.27

SI Table 2: The R23AW-SAND composite bulk composition was determined by total digestion. Samples were weighed out in PFA digestion liners on a balance with 0.1 mg resolution. The following were then added to the liners: 3 mL hydrofluoric acid (HF), 2 mL nitric acid (HNO_3), 1 mL hydrochloric acid (HCl), and 2 mL de-ionized water. All acids where ultra-high purity grade (BDH Aristar Ultra).Liners were capped, mounted in pressure vessels and put into microwave reaction system (Anton PaarMultiwave 3000 with rotor 8SXF100) and digested at ~260*C and <1700 psi. This method used a maximum power of 1400W with 10 minute ramp time and 30 minute hold (digestion) time.

Upon digestion and cooling to ambient temperature, samples were transferred to a 10 mL PFA volumetric flask and diluted using de-ionized water. Each PFA flask was calibrated before use to minimize volume error. An aliquot from each digested sample was then diluted 50 times, spiked with internal standard (Li-6, Ga-71, Rh-103, Tm-169) and analyzed using a Perkin Elmer SCIEX Elan DRC II using a quantitative method.

Total extractable As concentrations for the cores which were used to create this sample are 2-4 nmol/g (0.15-0.30 ppm) and As is relatively uniformly distributed.[11] This means that for the 0.5 hr As(III)-treated sample, ~50% of As is native and 50% from added As. For the 24-hr As(III)-treated sample it's about 95% added As and 5% native.

Element	Concentration (μg/g)	Uncertainty (μg/g)
Na	2,200	353
Mg	343	35
Al	8,970	633
Si	497,000	34,100
K	5,970	427
V	7.28	0.44
Cr	3.31	0.26
Mn	29.6	1.5
Ca	352	21
Fe	3,600	229
Ti	531	31
Sr	16.70	2.35
Ba	103	6
Ce	5.53	0.78
Pb	4.39	0.37
Th	0.435	0.068
U	0.62	0.05

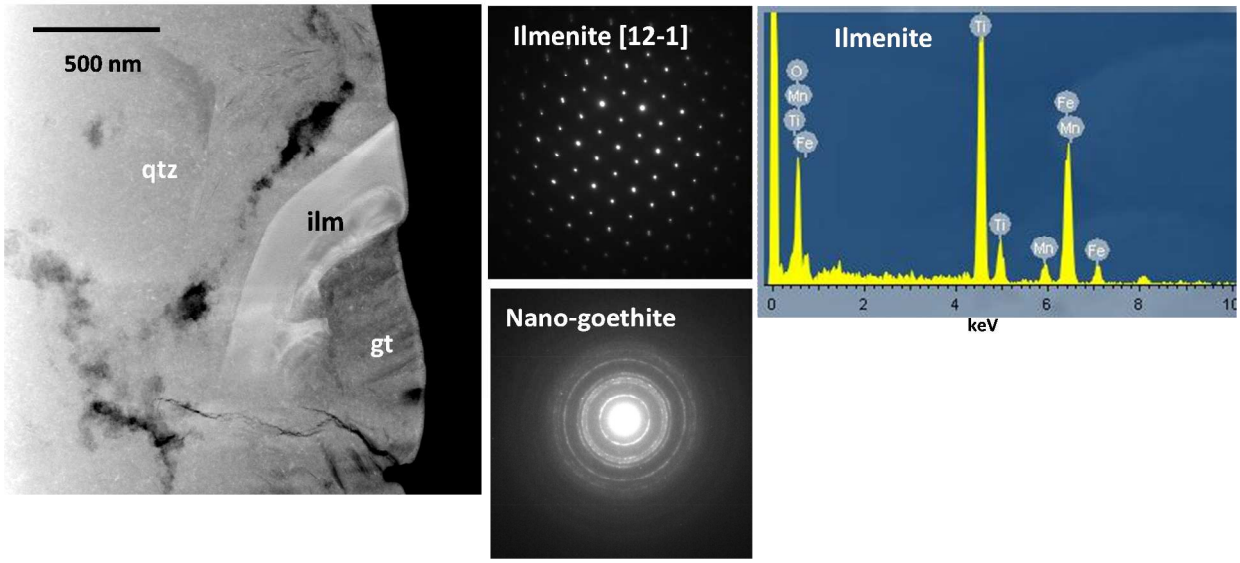

SI FIG 1: Additional TEM dark field image of a FIB-extracted grain coating (right), electron diffraction patterns (center) and an EDS spectrum highlighting the presence of both nanoparticulate goethite (gt) and ilmenite (ilm) in the mineral coatings. This sample was exposed to As(III) for 30 minutes.

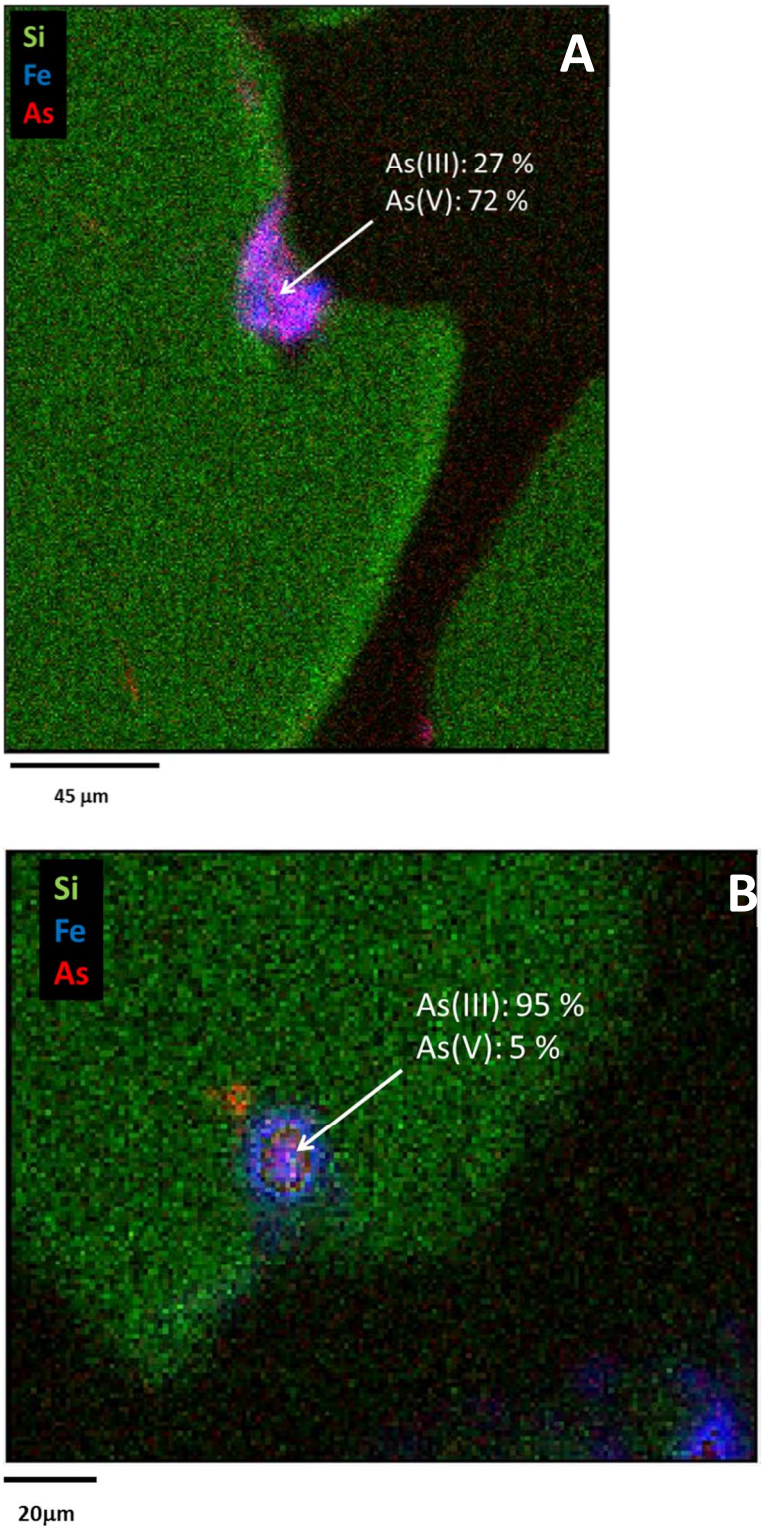

SI Figure 2. Additional XMP maps (SSRL) of two quartz grain edges in a polished thin section, showing Fe and As fluorescence and As redox speciation. The arrow points to the approximate location where micro-XANES spectra were collected. This sample was exposed to As(III) for 30 minutes.

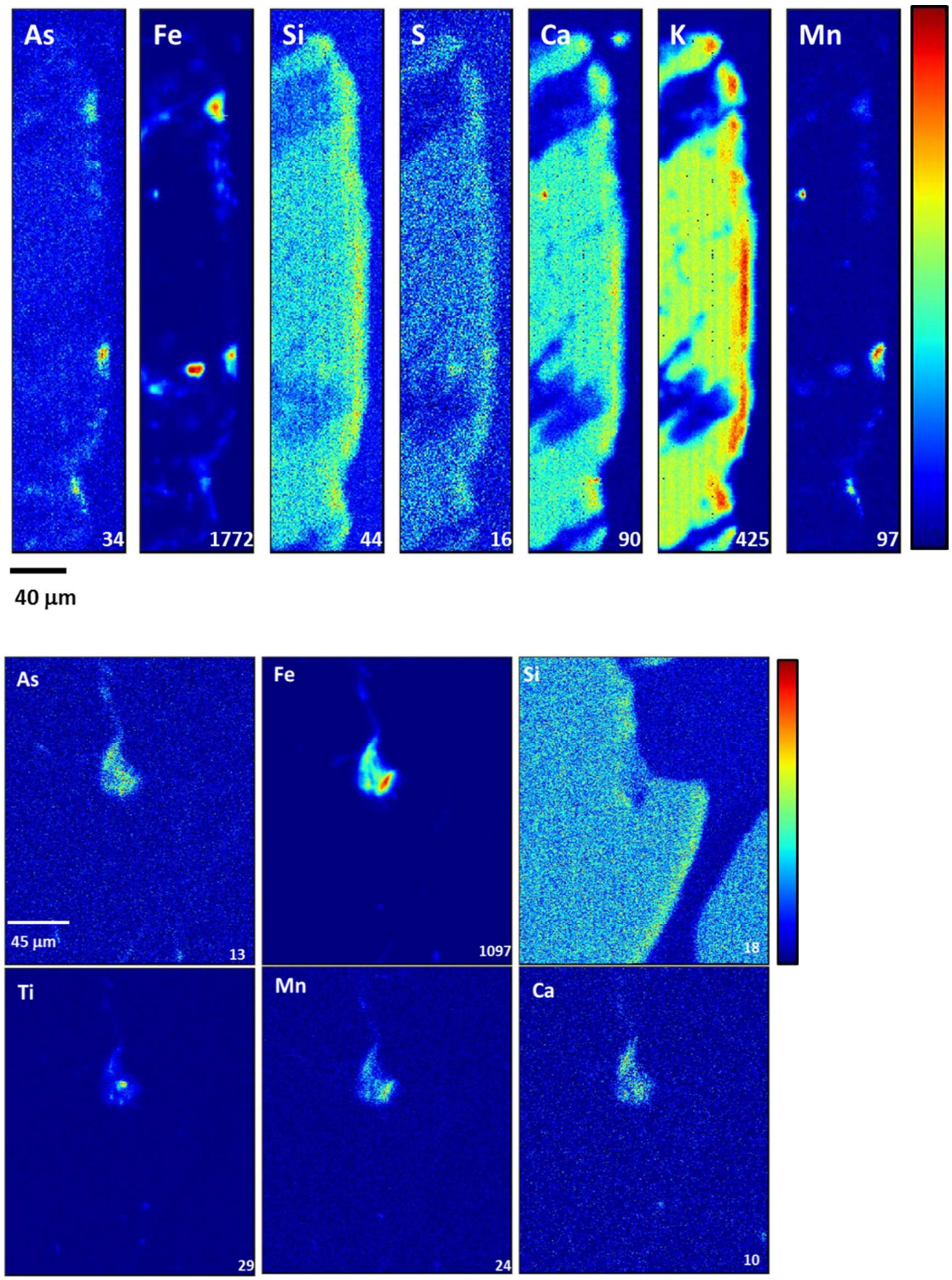

SI Figure 3. Additional XMP element maps (SSRL) of R23AW-SAND after exposure to $As(III)_{aq}$ for 30 minutes. The maps show the edges of two quartz grains in polished thin sections. The numbers in the lower right corner of each map are the maximum fluorescence count value corresponding to the color legends at right; minimum values are zero counts.

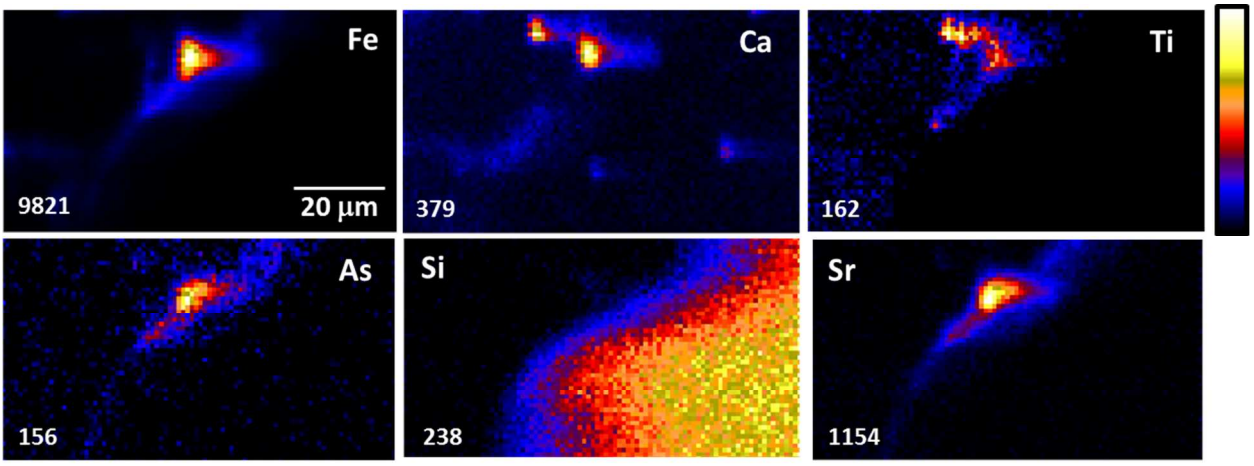

SI Figure 4. Additional XMP element maps (APS) of R23AW-SAND after exposure to $As(III)_{aq}$ for 2 hours. The maps show the edge of one quartz grain in a polished thin section. The numbers in the lower left corner of each map are the maximum fluorescence count value corresponding to the color legends at right; minimum values are zero counts. XMP data were acquired with procedures similar to those described in Newville et al. (1999).[12]

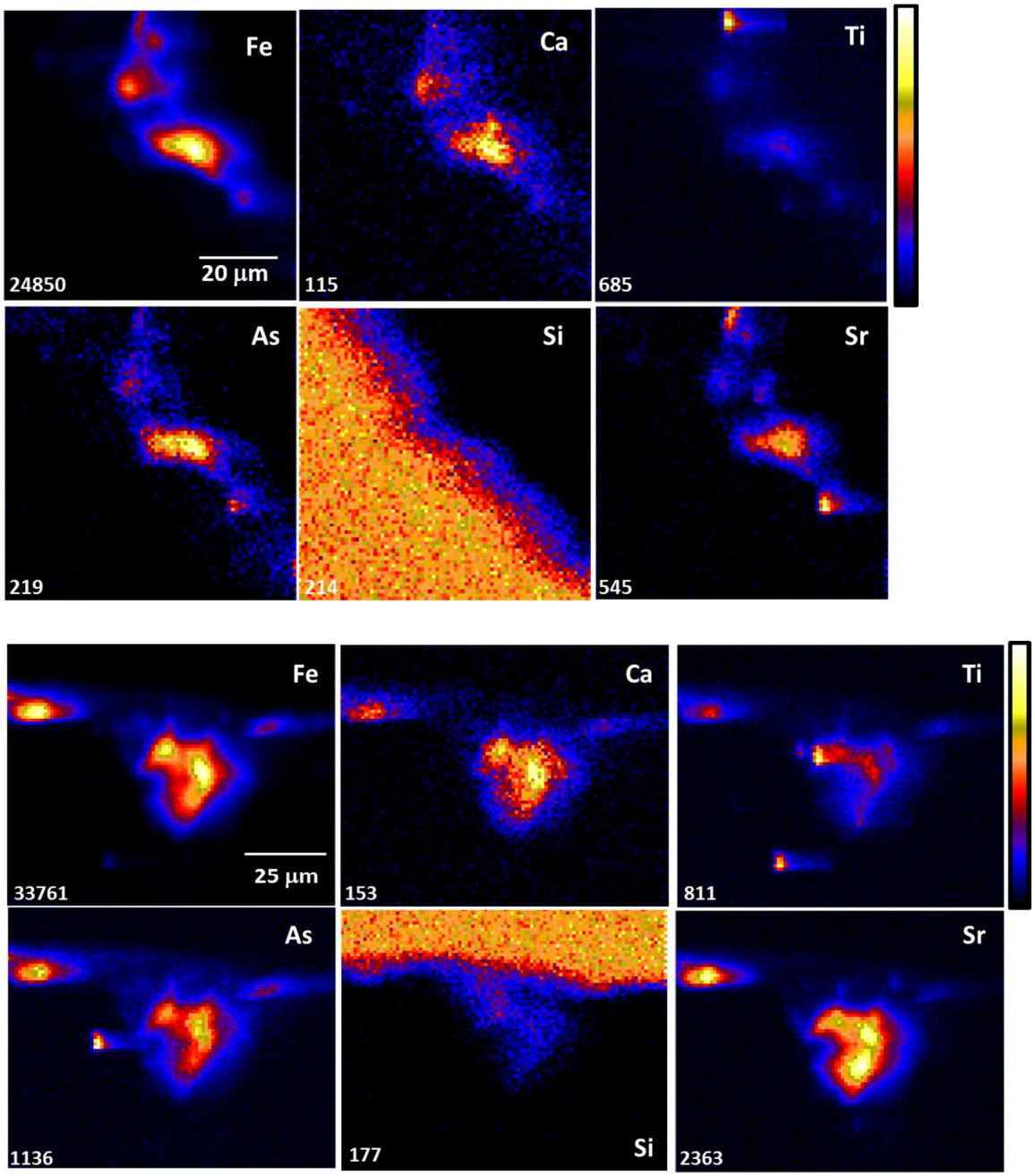

SI Figure 5. Additional XMP element maps (APS) of R23AW-SAND after exposure to $As(III)_{aq}$ for 24 hours. The maps show the edges of two quartz grains in polished thin sections. The numbers in the lower left corner of each map are the maximum fluorescence count value corresponding to the color legends at right; minimum values are zero counts.

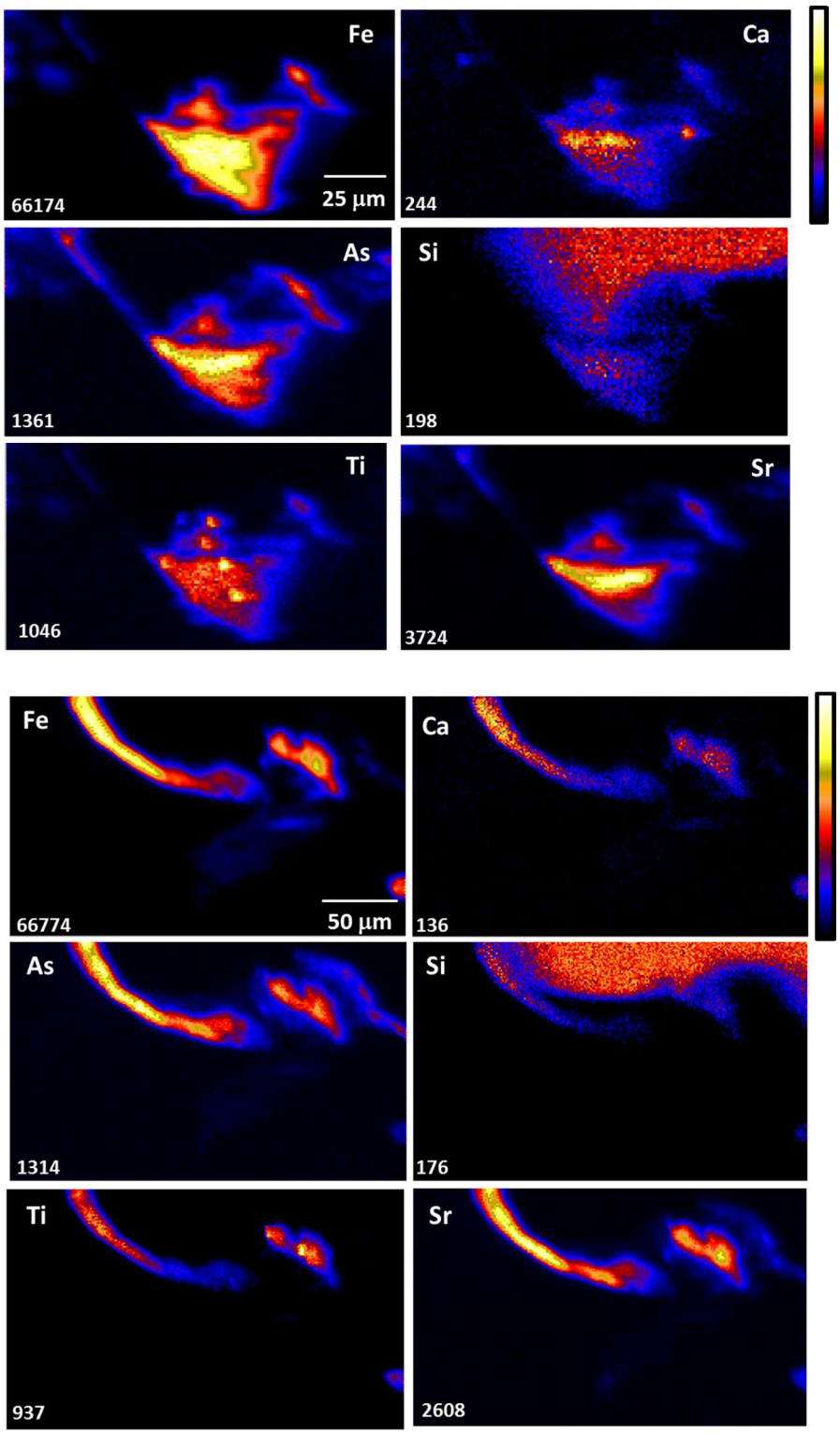

SI Figure 6. Additional XMP element maps (APS) of R23AW-SAND after exposure to $As(V)_{aq}$ for 24 hours. The maps show the edges of two quartz grains in polished thin sections. The numbers in the lower left corner of each map are the maximum fluorescence count value corresponding to the color legends at right; minimum values are zero counts.

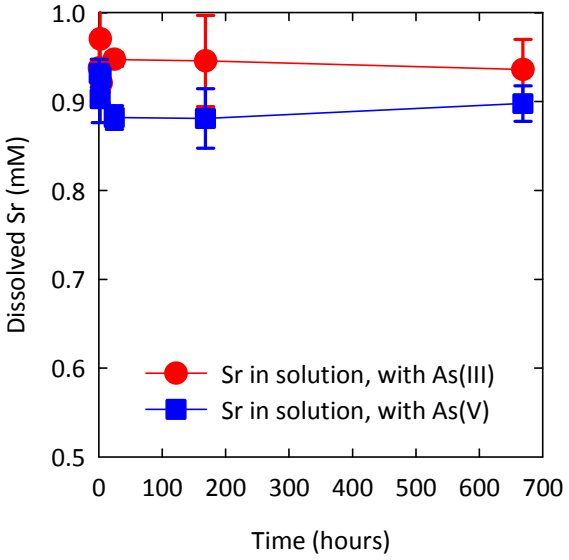

SI Figure 7. Strontium batch sorption results versus time showing dissolved Sr remaining in solution in As(III)- and As(V)-bearing solutions; error bars represent two standard deviation values.

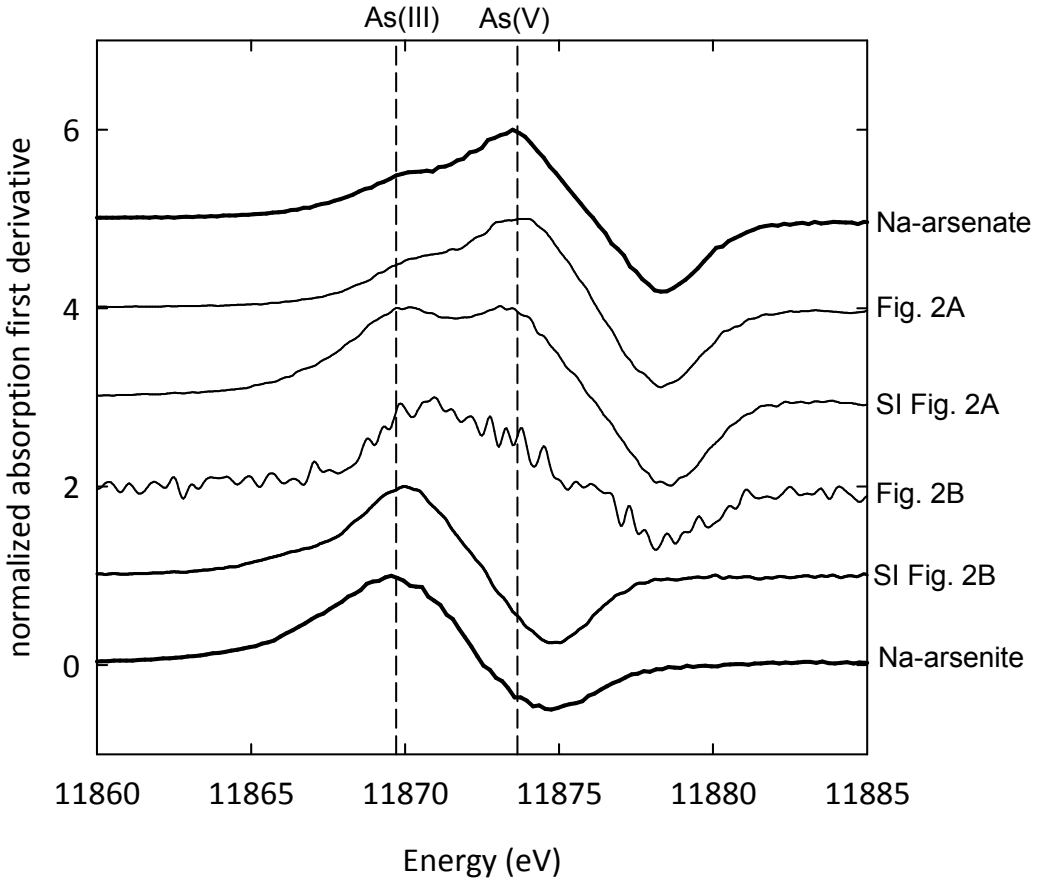

SI Figure 8: First derivative micro-XANES spectra. Location labels refer to the approximate location of where the arrows point in the respective figures. Sodium arsenite and sodium arsenate were used as As(III) and As(V) standards, respectively.

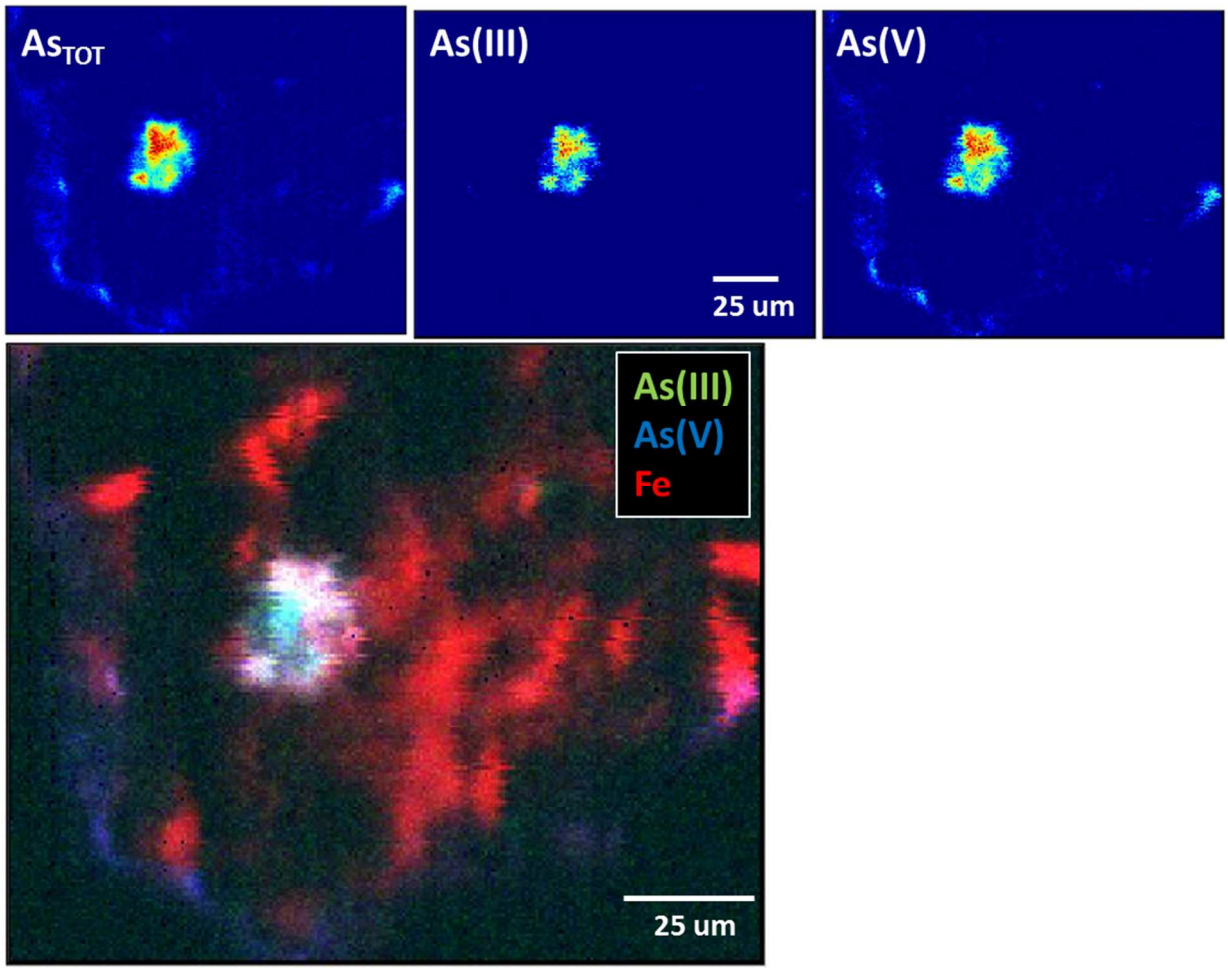

SI Figure 9. Arsenic redox XMP images based on maps collected at 11860 eV, 11872 eV, 11875 eV, and 11880 eV to determine the distribution of As(III) and As(V) and at 15000 eV for Fe spatial distribution. The maps show the edges and interior of a quartz grain in a polished thin section. This sample was exposed to As(III) for 30 minutes. The "whitish" area near the center is an artifact of overlapping distributions of As(III), As(V), and Fe near their maximum fluorescence counts in this image.

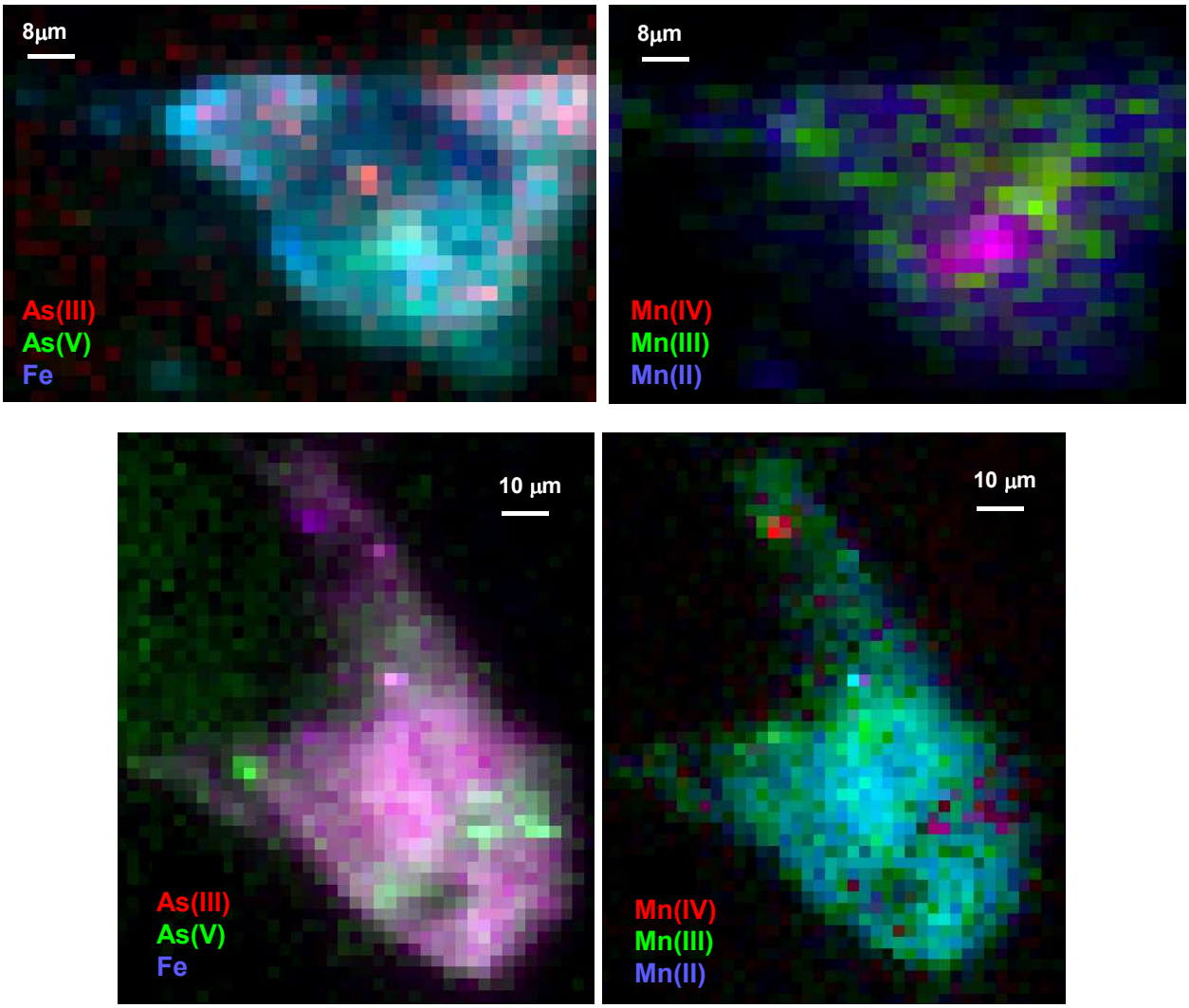

SI Figure 10. Arsenic (left) and manganese (right) redox maps and total Fe spatial distribution collected at the Advanced Light Source, beamline 10.3.2, on the edges of two grains of a polished thin section. This sample was exposed to As(III) for 30 minutes.

References

1. Webb, S. M., The MicroAnalysis Toolkit: X-ray Fluorescence Image Processing Software. *AIP Conference Proceedings* **2011,** *1365*, 196-199.
2. Webb, S., SixPACK: a graphical user interface for XAS analysis using IFEFFIT. *Phys. Scr.* **2005,** *T115*, 1011-1014.
3. Masue-Slowey, Y.; Kocar, B. D.; Bea Jofré, S. A. s.; Mayer, K. U.; Fendorf, S., Transport Implications Resulting from Internal Redistribution of Arsenic and Iron within Constructed Soil Aggregates. *Environ. Sci. Technol.* **2010,** *45*, (2), 582-588.
4. Ying, S. C.; Masue-Slowey, Y.; Kocar, B. D.; Griffis, S. D.; Webb, S.; Marcus, M. A.; Francis, C. A.; Fendorf, S., Distributed microbially- and chemically-mediated redox processes controlling arsenic dynamics within Mn-/Fe-oxide constructed aggregates. *Geochim. Cosmochim. Acta* **2013,** *104*, (0), 29-41.
5. Marcus, M. A., X-ray photon-in/photon-out methods for chemical imaging. *"TrAC, Trends Anal. Chem. "* **2010,** *29*, (6), 508-517.
6. Manceau, A.; Marcus, M. A.; Grangeon, S., Determination of Mn valence states in mixed-valent manganates by XANES spectroscopy. *Am. Mineral.* **2012,** *97*, (5-6), 816-827.
7. Arai, Y.; Lanzirotti, A.; Sutton, S.; Davis, J. A.; Sparks, D. L., Arsenic Speciation and Reactivity in Poultry Litter. *Environ. Sci. Technol.* **2003,** *37*, (18), 4083-4090.
8. Seyfferth, A. L.; Webb, S. M.; Andrews, J. C.; Fendorf, S., Defining the distribution of arsenic species and plant nutrients in rice (Oryza sativa L.) from the root to the grain. *Geochim. Cosmochim. Acta* **2011,** *75*, (21), 6655-6671.
9. Strawn, D.; Doner, H.; Zavarin, M.; McHugo, S., Microscale investigation into the geochemistry of arsenic, selenium, and iron in soil developed in pyritic shale materials. *Geoderma* **2002,** *108*, (3–4), 237-257.
10. Zhuang, Y.; Ahn, S.; Seyfferth, A. L.; Masue-Slowey, Y.; Fendorf, S.; Luthy, R. G., Dehalogenation of Polybrominated Diphenyl Ethers and Polychlorinated Biphenyl by Bimetallic, Impregnated, and Nanoscale Zerovalent Iron. *Environ. Sci. Technol.* **2011,** *45*, (11), 4896-4903.
11. Kent, D.; Fox, P., The influence of groundwater chemistry on arsenic concentrations and speciation in a quartz sand and gravel aquifer. *Geochem. Trans.* **2004,** *5*, (1), 1-12.
12. Newville, M.; Sutton, S. R.; Rivers, M. L.; Eng, P., Micro-beam x-ray absorption and fluorescence spectroscopies at GSECARS: APS beamline 13ID. *J. Synchrotron Rad.* **1999,** *6*, (3), 353-355.